Propellant cohesive fracture during the peel test of a propellant/liner structure

Paul-Aymé Toulemonde, Julie Diani, Pierre Gilormini, Nancy Desgardin, Robert Nevière

Propellant cohesive fracture during the peel test of a propellant/liner structure

Paul-Aymé Toulemonde[a,b], Julie Diani[c], Pierre Gilormini[a], Nancy Desgardin[b], and Robert Nevière[b]

[a]Laboratoire PIMM, ENSAM, CNRS, CNAM, Paris, France; [b]Airbus Safran Launchers, Centre de recherche du Bouchet, Vert-le-Petit, France; [c]LMS, Ecole Polytechnique, CNRS, Université Paris-Saclay, Palaiseau, France

ABSTRACT

The integrity of propellant/liner structures in rocket motors is critical to ensure controlled combustion of the engine. In an effort to improve the bonding between the liner and the propellant, it is necessary to characterize it well. Therefore, a propellant–liner structure, bounded thanks to co-curing, has been submitted to a peel test while recording the macroscopic fracture energy and the local displacement field on the propellant-free surface. The experimental setup includes two cameras in order to record the displacement field on the propellant-free surface. Upon loading, the peel force stabilizes quickly due to a cohesive fracture in the propellant, providing access to the fracture energy. While the crack propagates through the propellant, it is observed that only a small localized area is submitted to strain, and most of the structure remains unstrained.

KEYWORDS

Aerospace; peel; rubbers

1. Introduction

The design of rocket motors includes a rubber layer in contact with the metal or composite motor case that acts as an insulation interface preventing excessive heating of the case during propellant combustion. This rubber layer is adhered to the propellant, thanks to a flexible liner. Strong adhesion between the liner and the propellant is targeted in order to prevent the appearance of voids or cracks within the propellant, which could appear during storage or transport for instance and could cause the failure of the engine. Therefore, the propellant/liner bond is a critical feature for the design of rocket motors. From a material point of view, strategies have been found to strengthen this joint [1,2]. In order to characterize the propellant/liner structure mechanically, several experimental tests including classic mode I fracture tests, poker-chip test, *etc.* [3], double-cantilever sandwich [4], and sandwich single lap

CONTACT Paul-Aymé Toulemonde patoulemonde@gmail.com Toulemonde, Laboratoire PIMM, ENSAM, CNRS, CNAM, 151 bd de l'Hôpital, 75013 Paris, France.

joint [5] were performed to assess the adhesive and cohesive fracture energies. These studies provide macroscopic quantitative measurements of the energy needed to detach the liner from the propellant and in some cases, qualitative microscopic observations of the propellant cohesive fracture or propellant/liner debonding. In the present contribution, the propellant/liner bond is tested *via* a peel test. Such a test has been used for testing the adhesion of bonded composite-to-aluminium joints for instance [6]. Cohesive fracture within the propellant is observed when the liner and the propellant are well bonded. Propellants are highly filled rubbers (fillers volume ratio can exceed 80%), which can sustain large strains up to 60% before breaking when submitted to uniaxial tension. Their mechanical behaviour is complex showing nonlinear viscoelasticity with damage [7,8]. Consequently, it is legitimate to question the occurrence of large strains that could dissipate some energy during propellant/liner debonding and, as a consequence, increase the cohesive fracture energy. To access the local strain field, digital image correlation (DIC) is used. The non-contact method is based on the mapping of an image in a loaded state to an image in a reference state and has been successfully applied at the microscale and nanoscale (for instance [9,10]) and for finite deformations [11,12]. Despite an apparent simplicity in implementation, DIC results are sensitive to various parameters and must be studied with care. Numerous DIC codes can provide estimates of the strain field [13], its accuracy depending on the speckle, lights, cameras, and optics [10].

During the peel test, the fracture energy is deduced from the peel force, while the local state of strain on the propellant-free surface is monitored with two cameras. On the one hand, macroscale observations verify the 90° peel angle and provide the estimates of the strain field over the whole thickness of the propellant slab, while on the other hand, observations at the microscale allow following the crack propagation and measuring the strain field in front of it.

2. Material and experimental setup

The tested propellant is a plasticized glycidyl azide polymer-based binder highly filled with energetic (ammonium perchlorate and octogen) particles and the liner is a silica-filled hydroxyl-terminated polybutadiene (HTPB). A woven cloth has been added within the liner in order to use it as peel arm. The cloth does not affect the liner high flexibility but prevents its stretchability that would add undesired energy dissipation when pulled during the peel test. The liner is partially cured during 24 hr at 65°C. Then, the propellant is added and both materials are co-cured during 3 weeks at 40°C to promote adhesion at the interface. At the end, the liner/propellant

structure is cut with a saw into slabs 100 mm long, 25 mm wide, and 6 mm thick (5 mm propellant and 1 mm liner).

The largest propellant-free surface in the propellant/liner structure is bonded with a polyurethane glue to a steel plate in order to fix it easily to a friction free rolling bench mounted onto a Zwick/Roell (Ulm, Germany) Z020 tension machine to perform 90° angle peel test. The position of the bench is controlled with a manual hydraulic displacement actuator to ensure that the peel arm remains vertical. The peel rate is 25 mm/min. The peel force is recorded with a 2 kN Zwick/Roell load cell. Note that one could be tempted to choose to glue the liner on the steel plate and use the propellant as the peel arm in order to mimic the rocket motor structure. Actually, the poor flexibility of the propellant creates troubles to maintain the peel angle constant, rendering the fracture analysis much more complex.

Two cameras have been installed, one on each side of the structure. A scale representation of the recorded image frames is shown in Figure 1. At the macroscale, a texture was created with spray painting while at the smaller

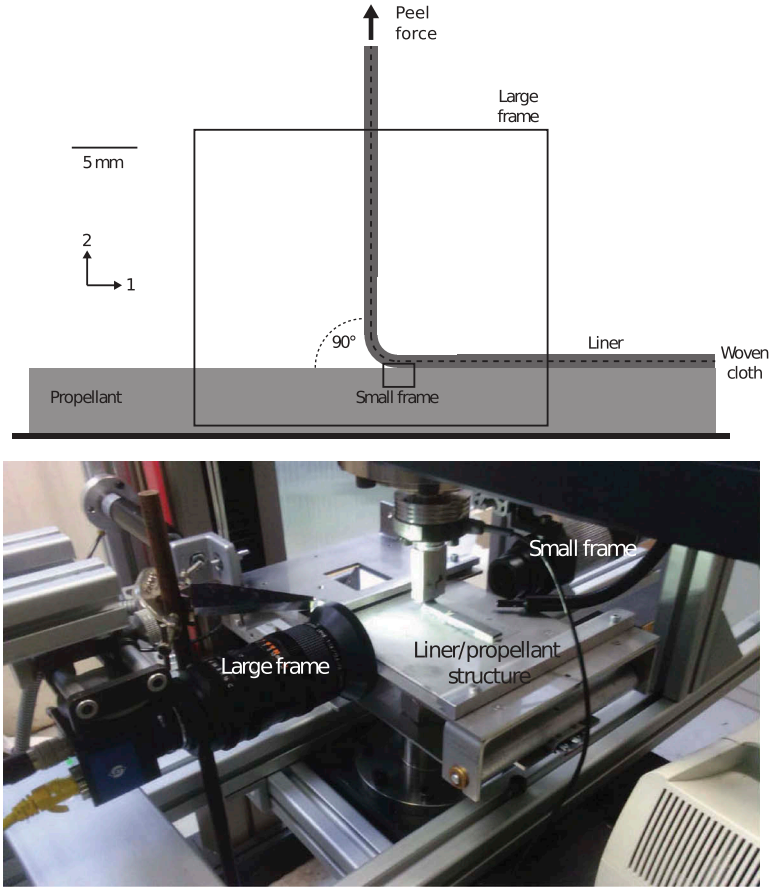

Figure 1. Experimental setup.

Table 1. Image acquisition systems.

	Small-frame images	Large-frame images
Camera	SVcam-eco267MVGE (Seefeld, Germany)	SVcam-eco655MVGE (Seefeld)
Frame size	1392 × 1040 pixels	2448 × 2050 pixels
Pixel size	1.7 microns	11 microns
Acquisition	12.5 Hz	2 Hz
Optics	Telecentric Moritex (Saitama, Japan) MLZ07545HRD	mm Computar (Cary, NC, USA) M6Z1212-3S

scale the presence of microscopic fillers ranging from 0 to 150 μm creates a natural speckle. Descriptions of the cameras and optics are given in Table 1.

Image mapping is performed with elastix v4.8 which is distributed as open source [14,15]. Element sizes of 16 × 16 pixels were used. The non-rigid transformations are defined by B-splines and a gradient descent optimization method is applied. From the estimated transformation $u(X)$ between two images, one estimates the in-plane deformation gradient tensor $F = 1 + \frac{\partial u}{\partial X}$. Finally, the Green–Lagrange strain tensor,

$$E = \frac{1}{2}\left(F^{\mathrm{T}}F - 1\right), \tag{1}$$

is calculated as the finite strain tensor. The three in-plane components of E and its magnitude will be used to present the strain field in the deformed state.

In order to examine the performance of the textures and optics, reference images were submitted to artificial unidirectional sinusoidal displacements along the vertical direction with various amplitudes and frequencies. A random noise defined by the difference between two reference images was also added to the sinusoidal transformations. Image correlation was applied between the reference image and the artificially modified images. Such a test allows testing a wider variety of displacement fields [13] that apply rigid body motions prior to the experiment [16]. As one could expect, the speckles performed well when the sinusoidal period was large (half of the image height) and so for a wide range of strain (Figure 2). The maximum positive strain applied (130%) was successfully reached, while compression values up to 40% were also satisfactorily attained. The main difficulty with high compressions is the “disappearance” of pixels. As one could expect, the performance of the speckles degrades significantly as the sinusoidal period decreases (Figure 2). Therefore, it will be possible to capture large strain, but qualitative results only are anticipated for high-strain gradient.

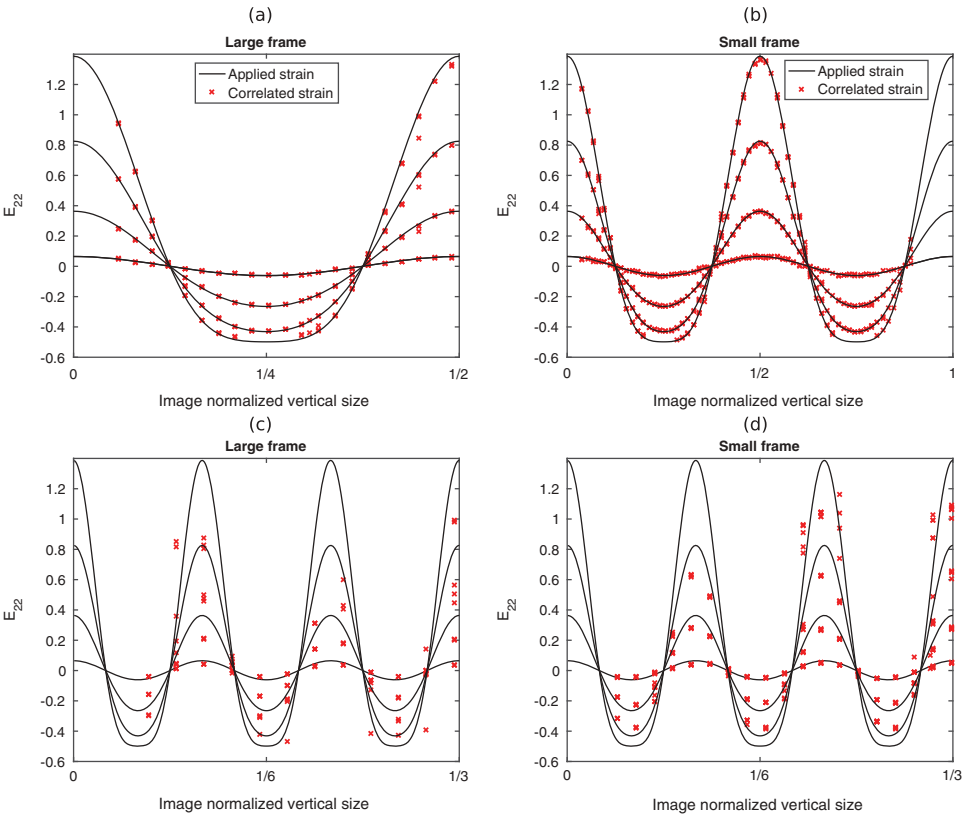

Figure 2. Speckle performances: comparison between artificially applied sinusoidal unidirectional pixel displacements and image correlation estimates for a large period of half the image size with (a) large-frame image (spray painting) and (b) small-frame image (natural texture) and for a small period of one-tenth of the image size with (c) large frame and (d) small frame.

3. Results

3.1. *Cohesive fracture energy*

During the peel test, the peel force is recorded over time. Figure 3 shows that after the initial increasing tension in the liner, the force reaches a plateau at 11 ± 1 N. This plateau exhibits the stable propagation of the peel process. Due to the low stretchability and high flexibility of the liner/cloth structure mentioned in Section 2, the fracture energy is easily evaluated by [17,18]:

$$W = F/b \tag{2}$$

with b being the width of the peel arm. Therefore, a fracture energy of $W = 440 \pm 40$ J.m^{-2} is obtained that is of the same order of magnitude as values reported for HTPB-based propellants [1]. The measured discrepancy can be due to the material inhomogeneity that may induce local variation of the fracture energy [19]. Finally, after propellant/liner

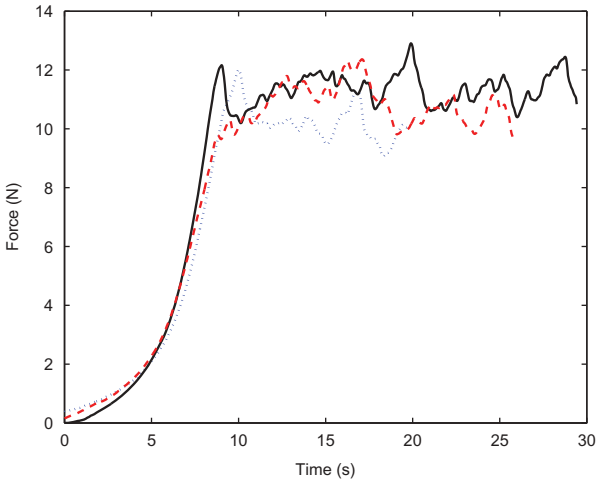

Figure 3. Peel force with respect to time recorded during three tests.

separation, a layer of propellant is witnessed on the liner, proving of a cohesive fracture in the propellant.

3.2. *Strain field*

In order to evaluate the strain field during the peel test, a first analysis is carried out on the large-frame images. A large part of the images being irrelevant, the

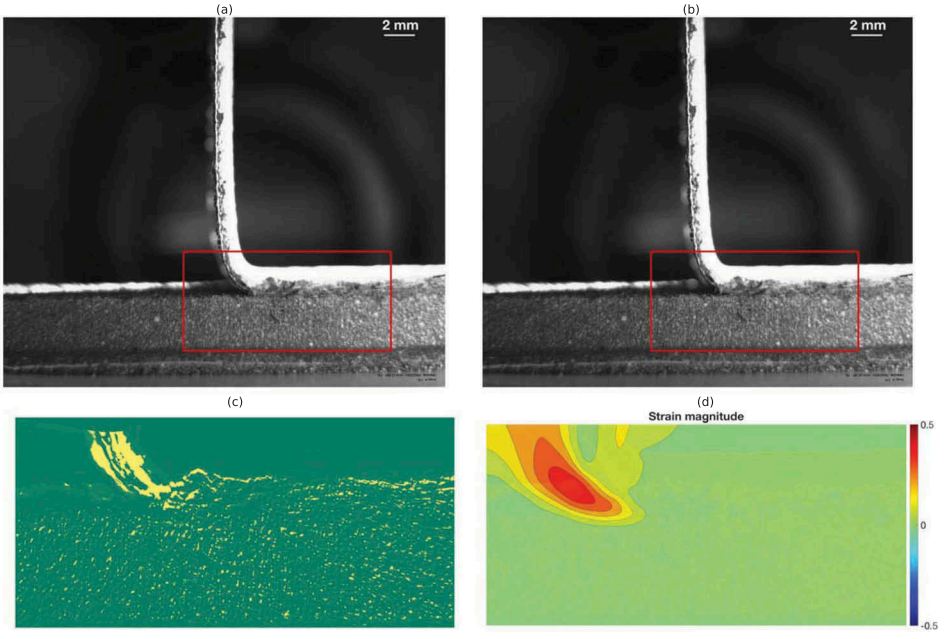

Figure 4. Example of digital image correlation on large-frame images: (a) reference image, (b) deformed image, (c) grey-level residual map after digital correlation, and (d) resulting strain magnitude.

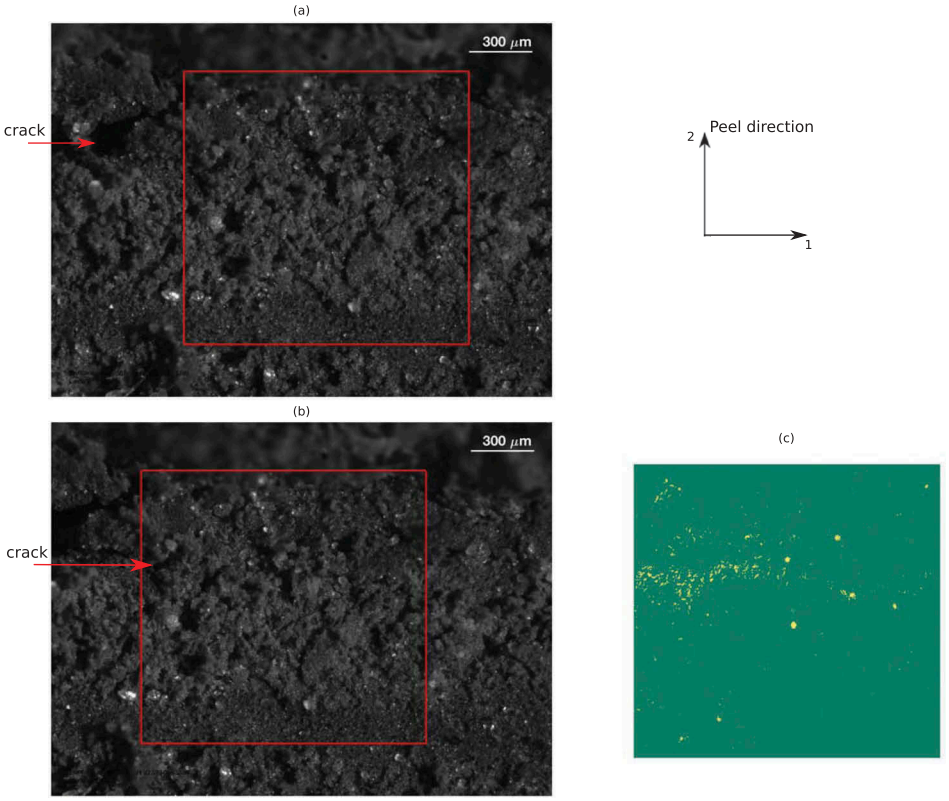

Figure 5. Example of digital image correlation on small-frame images: (a) reference image (the crack has not entered the red box yet), (b) deformed image (the crack has entered the box), and (c) grey-level residual map after image correlation.

DIC is carried out on reduced images which are the part of the images appearing in the red boxes in Figure 4. The DIC is performed between the reference image (Figure 4a) and the deformed image obtained 1.5 s later (Figure 4b). The difference between the reference image and the deformed image inversely transformed with the strain field calculated by DIC defines a residual map (Figure 4c). Here, such a map evaluates the DIC performance, and a good correlation is obtained where the picture is green while poor results were obtained in the spots of the yellow pixels. Therefore, the strain field obtained where the correlation is not satisfactory (indicated by yellow pixels in Figure 4c) is irrelevant. These areas of unsatisfactory correlation correspond to the orange and red areas displayed in Figure 4d. Analysing the rest of the image, the propellant slab seems to remain undeformed. Nonetheless, at this scale, the image definition is coarse and observation of the cohesive fracture of the propellant requires to zoom in. Thanks to the microscale images, a closer look is taken at the propellant/liner separation to follow the crack, while it propagates in the propellant. In order to better assess the strain field in front of

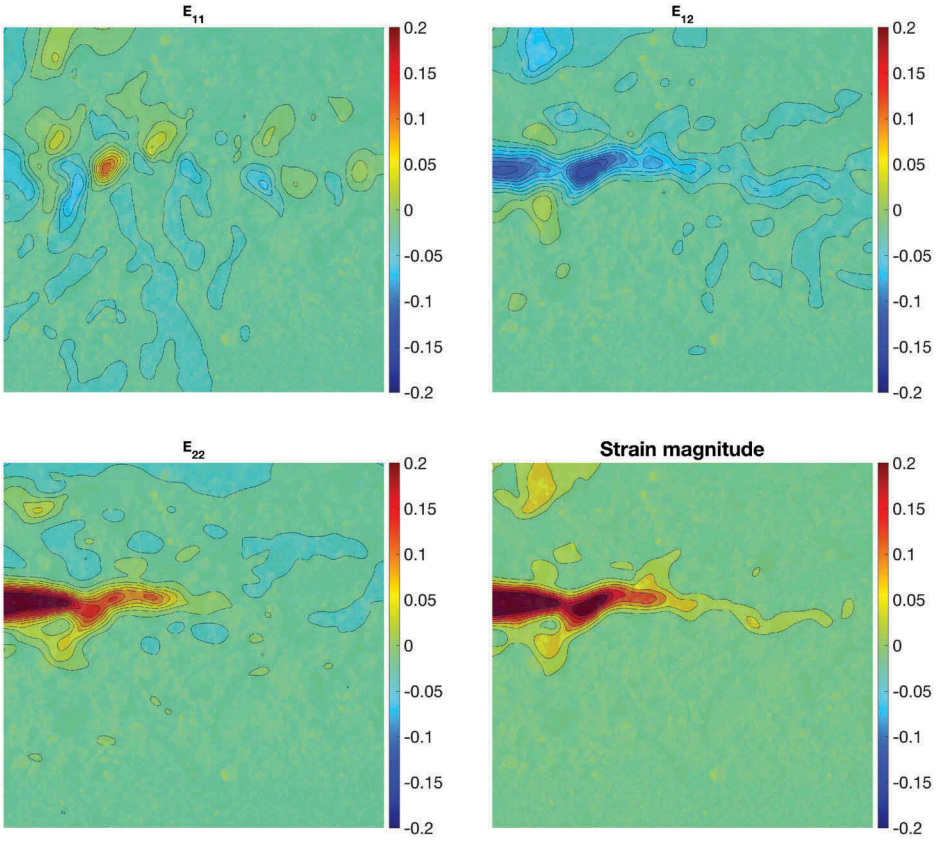

Figure 6. Strain field measured by Figure 5 image correlation.

the crack, DIC is applied to two small-frame images (Figure 5). One may note in Figure 5 the blurry part at the top of the image helping recognizing the limit between the propellant and the liner/cloth structure, the propellant appearing below this limit. As for the large frame images, a reduced part of the images, contained in the red boxes (Figure 5), is used for DIC. The residual map comparing the reference image and the inversely transformed deformed image allows identifying the crack path before the eye could recognize it, that is when the crack opens. The crack path is read on the residual map (Figure 5c). It is recognized by an unsatisfactory image correlation displayed by the yellow pixels. Apart from the crack area, DIC performed well since the residual map is mostly green. Consequently, the strain field in front of the crack tip is now discussed. The poor results obtained when the images were deformed artificially with a high-frequency sinusoidal signal (Figure 2) demand to be cautious with the estimates of the strain field in the close vicinity of the crack, where high-strain gradients are obtained. Figure 6 shows the estimated strain field when comparing the reference image and the deformed image presented in Figure 5. One reads that in front of the crack and in other areas of the image, the strain is

small and very often null. This result confirms what was observed in large-frame pictures: the propellant barely deforms during the peel test. As a consequence, for the propellant/binder structure tested, the propellant deformability and viscoelasticity do not help increasing its resistance to cohesive fracture. Finally, it appears that the distance between the crack and the liner is of the order of magnitude of 300 μm, which is consistent with the characteristic distance of chemical species migrations at the liner/propellant interface [20]. As shown in [21], cohesive fracture within the propellant is achieved when the right concentration of bond promoter is added due to reaction at the surface of ammonium perchlorate.

4. Conclusion

In order to characterize the bonding of a propellant/liner bond structure, an instrumented peel test of a propellant/liner structure was proposed. The main feature was to implement two-image acquisition chains recording the evolution of the propellant/liner separation at both the macro- and microscales while monitoring the peel force. It was observed that the propellant/liner separation was the result of a cohesive fracture within the propellant. At the macroscopic scale, the peel force reaches rapidly a plateau providing access to the propellant cohesive fracture energy. At a lower scale, the strain field observations proved that only a very localized area of propellant is submitted to strain. The fracture appears at a distance of the liner that is consistent with the chemical species migrations at the liner/propellant interface.

Funding

The authors acknowledge the financial support of DGA.

References

[1] Kakade, S. D., Navale, S. B., and Narsimhan, V. L., *J. Energ. Mat.* **21**, 73–85 (2003).
[2] Zhou, Q. C., Xu, J. S., Chen, X., and Zhou, C. S., *J. Adhes.* **92,** 402–428 (2016).
[3] Bills, K. W.Jr., and Schapery, R. A., *Technical Report*, (Aerojet Strategic Propulsion Company, Sacramento, CA, (1982).
[4] Zhou, Q. C., Ju, Y. T., Wei, Z., Han, B., and Zhou, C. S., *J. Adhes.* **90**, 230–251 (2014).
[5] Niu, R. M., Zhou, Q. C., Chen, X., Ju, Y.-T., Wei, Z., and Zheng, J., *Int. J. Adhes. Adhes.* **52**, 1–10 (2014).
[6] De Freitas, T. and Sinke, S., *J. Adhes.* **90**, 511–525 (2014).
[7] Azoug, A., Nevière, R., Pradeilles-Duval, R.-M., and Constantinescu, A., *J. Appl. Pol. Sci.* **131**, 40664 (2014).
[8] Oberth, A. E. and Bruenner, R. S., *Trans. Soc. Rheo.* **9**, 165–185 (1965).
[9] Knauss, W. G., Chasiotis, I., and Huang, H., *Mech. Mater.* **35**, 217–231 (2003).
[10] Berfield, T. A., Patel, J. K., Shimmin, R. G., Braun, P. V., Lambros, J., and Sottos, N. R., *Exp. Mech.* **47**, 51–62 (2007).

[11] Bergonnier, S., Hild, F., and Roux, S., *J. Strain Anal. Eng.* **40**, 185–198 (2005).
[12] Meunier, L., Chagnon, G., Favier, D., Orgéas, L., and Vacher, P., *Polym. Test.* **27**, 765–777 (2008).
[13] Bornert, M., Brémant, F., Doumalin, P., Dupré, J.-C., Fazzini, M., Grédiac, M., Hild, F., Mistou, S., Molimard, J., Orteu, J. J., Robert, L., Surrel, Y., Vacher, P., and Wattrisse, B., *Exp. Mech.* **49**, 353–370 (2009).
[14] Klein, S., Staring, M., Murphy, K., Viergever, M. A., and Pluim, J. P. W., *IEEE Trans. Med. Imaging.* **29**, 196–205 (2010).
[15] Shamonin, D. P., Bron, E. E., Lelieveldt, B. P. F., Smits, M., Klein, S., and Staring, M., *Front. Neuroinform.* **7**, 1–15 (2014).
[16] Hild, F. and Roux, S., *Strain*. **42**, 69–80 (2006).
[17] Rivlin, R. S., *Paint. Technol.* **9**, 2611–2614 (1944).
[18] Lindley, P. B., *J. Inst. Rubber Ind.* **5**, 1186–1195 (1971).
[19] Xia, S., Ponson, L., Ravichandran, G., and Bhattacharya, K., *Phys. Rev. Lett.* **108**, 196101 (2012).
[20] Huang, Z.-P., Nie, H.-Y., Zhang, Y.-Y., Tan, L.-M., Yin, H.-L., and Ma, X.-G., *J. Hazard. Mat.* **229–230**, 251–257 (2012).
[21] Gercel, G. O., Üner, D. O., Pekel, F., and Özkar, S., *J. Appl. Polym. Sci.* **80**, 806–814 (2001).